AIAA 2001–2962

Aerothermodynamic Characteristics in the Hypersonic Continuum-Rarefied Transitional Regime

Christopher E. Glass and James N. Moss
NASA Langley Research Center, Aerothermodynamics Branch, Hampton, VA 23681-2199

35th AIAA Thermophysics Conference
June 11–14, 2001/Anaheim, CA

Aerothermodynamic Characteristics in the Hypersonic Continuum-Rarefied Transitional Regime

Christopher E. Glass* and James N. Moss†
NASA Langley Research Center, Aerothermodynamics Branch, Hampton, VA 23681-2199

Stagnation pressure and heating for cylinders and spheres representative of wing leading edges and nose sections for small-scale space transportation vehicles are presented for various Knudsen numbers at Earth entry conditions that bridge from the free molecular to continuum regimes. CFD, DSMC, and collisionless DSMC are used to span Knudsen numbers from 0.001 to 100 with the CFD/DSMC overlap at a Knudsen number of 0.01 and the DSMC/collisionless DSMC overlap at 10. The present results include density contours, density and temperature along the stagnation streamline for all cases, and stagnation pressure and heat transfer coefficient as a function of Knudsen number.

Nomenclature

C_H	Heat transfer coefficient, $\dot{q}''/\frac{1}{2}\rho_\infty V_\infty^3$
C_p	Pressure coefficient, $(p-p_\infty)/\frac{1}{2}\rho_\infty V_\infty^2$
D	Diameter, m
Kn_D	Knudsen number based on diameter, D
p	Pressure, Pa
$\dot{q}''$	Heat transfer rate, W/m^2
R	Radius, m
T	Temperature, K
V	Velocity, m/s
x, y, z	Cartesian coordinate system, m
Z	Geometric altitude, km
ρ	Density, kg/m^3

Subscripts

ov	Overall, associated with all modes
tran	Translational
rot	Rotational
vib	Vibrational
w	Wall
∞	Free stream

Introduction

ACCURATE and credible prediction of three-dimensional leading edge aerothermodynamic characteristics in the transitional flow regime at and near rarefied flight conditions bridging from continuum to rarefied flow is a challenge. For small-scale space transportation vehicles, including small experimental X-vehicles, crew transfer vehicles (CTV), or crew and cargo transfer vehicles (CCTV), and future air breathing vehicles having extremely sharp leading edges, rarefaction phenomena are extremely important as maximum heating may occur on leading edges in the rarefied, as opposed to continuum, regime. Also, heating loads may be different than inferred from continuum approaches. These mispredictions in the aerothermal environment may have corresponding negative effects in the TPS material selection and sizing.

For predicting the flight aerothermodynamics in the transitional flow regime, numerical techniques are relied on to a greater extent to define leading edge flow field and surface effects than experimental techniques. Few experimental rarefied flow facilities are available to test models representative of complex, three-dimensional space transportation vehicles. Also, for most experimental wind tunnel model scales of these vehicles, leading edge dimensions do not lend to accurate discrete measurements because the sensor size is of the same magnitude as the leading edge and, for a single data point, integrates the loads over a significant portion of the leading edge. Three-dimensional heat conduction affects small model leading edge measurements because it diffuses the flow induced heating and reduces the maximum heating value. Also, global leading edge measurement techniques that visualize the surface, such as pressure sensitive paint, infrared thermography, or thermographic phosphors, suffer from rapid pixel-to-pixel viewing angle changes, insufficient pixel coverage, and three-dimensional conduction as with discrete heat transfer measurements.

Numerical techniques also have their limitations, which must be addressed. Commonly used numerical techniques to provide aerothermodynamic estimates in the transitional flow regime at and near rarefied flow conditions are computational fluid dynamics[1] (CFD) and direct simulation Monte Carlo[2] (DSMC). In gen-

*Research Engineer, AIAA Senior Member.

†Research Engineer, AIAA Fellow.

eral, CFD is applicable to the continuum regime, although with some approximations to the near surface flow, it can provide solutions into the transitional flow regime. Additionally, CFD offers a complication of finely gridding the flow about leading edges, which produce large flow gradients, and joining these regions to coarser gridding over acreage regions of the body.

Of available numerical techniques, DSMC offers the most accurate and credible solution method for the rarefied and near rarefied condition. However, because the method is probabilistic, i.e., it tracks movements and collisions of simulated molecules and statistically samples the positions and surface interactions, it requires long run times on a computer. In addition, as the flow condition approaches the continuum from the rarefied regime, the DSMC method requires many more simulated molecules and the attendant larger computer memory and longer CPU run times. Yet this computer hardware restriction has recently been diminished with the introduction of larger multi-processor computers and DSMC software written specifically for three-dimensional problems using parallel processing algorithms to take advantage of multi-processor computer architectures.

Motivation

The intent of this study is to employ a three-dimensional DSMC algorithm[3] to assess its usefulness in providing three-dimensional leading edge flow field and surface solutions for flow at and near rarefied flight conditions with application to current and future aerospace vehicles. The particular issues that are investigated in this study are verifying the three-dimensional DSMC results by comparison with a validated 2-D/axisymmetric DSMC algorithm[1] and CFD algorithm,[5] determining the bridging relationship of the stagnation point values over a range of Kn_D from continuum to free molecular, and providing guidance for the transition from CFD to DSMC and from DSMC to collisionless DSMC.

By verifying the three-dimensional results in the transitional flow regime, greater acceptance will be gained in applying the DSMC technique to obtain aerothermodynamic definition on leading edges, where the technique more closely represents the flow physics than the the current CFD options. As computer capability increases both in speed and memory, three-dimensional DSMC will become the defacto method for near rarefied transitional flow regime solutions, and verification of the technique, such as performed in this study, will prove useful in providing confidence in extending the applicable Kn_D range of DSMC.

In addition, results of this study will be useful in providing applicability limits of CFD, DSMC, and collisionless DSMC techniques. In the present study, CFD is performed for $Kn_D = 0.001$ and 0.01, DSMC for $0.01 \leq Kn_D \leq 10$, and collisionless DSMC for $Kn_D = 10$ and 100. At $Kn_D = 0.01$, CFD and DSMC results overlap, and at $Kn_D = 10$, DSMC and collisionless DSMC results overlap. The flow regime changes from continuum to transitional and from transitional to free molecular, respectively, near these Knudsen numbers, and by performing overlap calculations at these conditions and analyzing the results, the suitability of each technique at the overlap can be assessed.

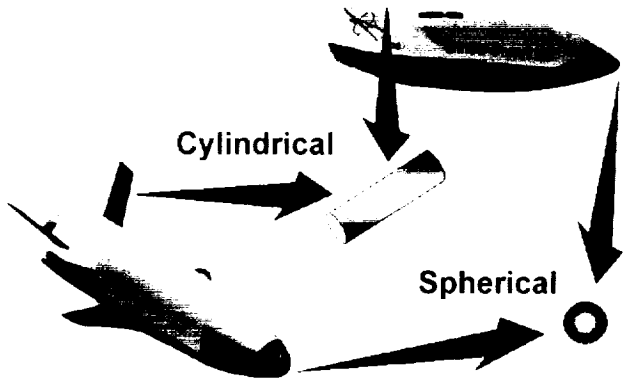

Fig. 1 Similarity between simple geometric shapes and wing leading edges and nose sections of small-scale space transportation vehicles.

Methodology

For this study, the strategy chosen is to apply 2-D and 3-D CFD and DSMC techniques to simple cylindrical and spherical geometries at various flight conditions that span $0.001 < Kn_D < 100$. Shown in Figure 1 are two flight vehicles that are designed to travel through this transitional regime. Also shown on the figure is the geometric similarity between a cylinder and sphere, which are presently studied, and wing leading edges and nose sections.

A diameter of $D = 0.1$ m was chosen for this study because it is close to the wing diameter of the small-scale space transportation vehicles shown in Figure 1. Further, the wall is assumed noncatalytic with a $T_w = 300$ K to produce large temperature variation through the shock layer and to exercise the techniques to a greater extent near the wall. For all cases, a constant velocity of $V_\infty = 6000$ m/s is specified, the air properties and composition was obtained from the 1976 U.S. Standard Atmosphere,[6] and reacting gas chemistry is utilized. Table 1 shows free stream conditions at various altitudes taken from the standard atmosphere.

A sketch of the coordinate system for the cylinder and sphere numerical solutions is presented in Figure 2. Note that the cylinder and sphere are centered in the x, y, z system with the free stream flow proceeding in the x-direction. Also, in the results presented subsequently, the coordinates are normalized by the radius, R.

Table 1 Free stream conditions for the Kn_D range.

Kn_D	Z, km	T_∞, K	ρ_∞, kg/m^3	p_∞, Pa
0.001	51.9	269.2	8.130 x 10^{-4}	62.83
0.01	70.5	219.2	7.722 x 10^{-5}	4.837
0.1	84.0	188.6	8.051 x 10^{-6}	0.4360
1	98.0	191.7	8.071 x 10^{-7}	0.04506
10	111.4	256.3	7.657 x 10^{-8}	0.006009
100	132.0	488.7	6.904 x 10^{-9}	0.001109

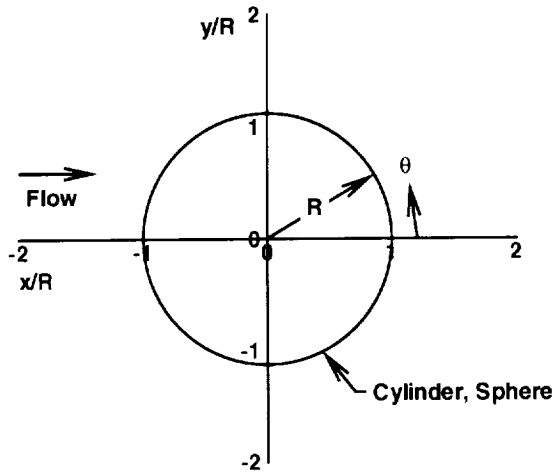

Fig. 2 Cylinder and sphere coordinate system.

As mentioned previously, the molecular analysis is performed by the DSMC Analysis Code (DAC),[3] which is a three-dimensional code with both scalar and parallel processing options. DAC has achieved a significant acceptance for rarefied three-dimensional applications. The parallel version is currently employed to produce DSMC solutions over the majority of the Kn_D range. Collisionless DSMC provides solutions in the high Kn_D region; G2 code[4] results are utilized to anchor and verify DAC results throughout the the Kn_D range; and GASP[5] CFD provides continuum solutions and bridges to the near continuum DAC results. Table 2 presents the numerical technique and

Table 2 Numerical technique and code for cylinder and sphere results.

Kn_D	CFD	DSMC	Collisionless DSMC
0.001	GASP		
0.01	GASP	DAC,G2	
0.1		DAC	
1.0		DAC,G2	
10		DAC,G2	DAC
100			DAC

specific computer code used to provide solutions for the various Knudsen numbers. As shown in the table, the number of flow solutions is 11 each for the cylinder and sphere.

The DAC code requires a triangulated surface grid of the body of interest, which is then positioned into a Cartesian flow field grid, for the DSMC solution. In this study, the 2-D, axisymmetric, and 3-D options of the DAC code were exercised. Therefore, three surface grids were built for the DSMC portion of the study, one for the cylinder and two for the sphere. In addition, the DSMC solutions included the wake region so that the entire surface geometry was modeled. The surface grid for the 2-D cylinder consisted of 360 triangles to completely enclose the geometry, and the sphere was composed of 12,363 surface triangles. Note that a 5° slice of the sphere with 146 triangular elements is the geometry for the axisymmetric DAC case ($Kn_D = 0.01$).

Both the cylinder and sphere CFD solutions were only about the windward portion of the geometry and the outflow boundary condition used is an extrapolation from the interior, which is appropriate because the flow exiting the grid is supersonic. Because the solution was 2-D, the grid used for the cylinder consists of 257x361x2 points with 257 points away from the wall. For the sphere, the grid is composed of two blocks. The block with the stagnation region is a 37x37x81 point block with 81 points away from the wall. The stagnation region block was constructed with no singularity at the stagnation point so that difficulties associated with solutions about a singular point were avoided. The second block of the sphere flow field patched the stagnation region with the outflow boundary. For both geometries, the grid normal to the wall is closely clustered to resolve the large gradients at the stagnation point and spacing proceeds away from the wall with an exponential factor of $\beta = 1.001$.

Fully reacting chemistry models are used for both the DSMC and CFD solutions. DAC solutions employ translational, rotational, vibrational, and chemical energy transfer modes between six molecules and atoms (N_2, O_2, NO, N, O, and Ar). The present application of DAC uses rotational and vibrational relaxation numbers of 5 and 50, respectively. GASP CFD solutions utilize the non-equilibrium, finite-rate, 5-specie (N_2, O_2, NO, N, and O) chemistry model of Kang and Dunn with vibrational energy taken into account for the three diatomic molecules.

Results and Discussion

This section presents results from the 22 flow solutions that are given in Table 2. Discussed in the first section is numerical uncertainty of the molecular and continuum techniques. Next, results consisting of flow field density contours, temperature and density variation along the stagnation streamline from the free stream condition to the wall, maximum atomic oxygen and nitrogen along the streamline, temperature (overall, translational, rotational, and vibrational) variation

along the stagnation streamline for the $Kn_D = 0.01$ case, and the stagnation pressure and heating are given. The contours will show the effect of rarefaction of the overall flow field. Presented next, temperature and density along the stagnation streamline more clearly show the effect of varying Knudsen number on the shock layer structure. Also, along the stagnation streamline, the maximum mole fraction of atomic oxygen and nitrogen and the overall, translational, rotational, and vibrational temperature mode distribution will allow an assessment of the degree of chemical and thermal nonequilibrium of the flow. Finally, the stagnation pressure and heating as a function Knudsen number will exhibit the degree of agreement between the various techniques and the bridging of these surface properties from the continuum to the rarefied regime.

Properties presented in this section are normalized by an appropriate factor. Temperature and density are normalized by the free stream values given in Table 1. The normalization factors for C_p and C_H are given in Table 3.

Table 3 Normalization factors for C_p and C_H.

Kn_D	p_∞	$1/2\rho_\infty V_\infty^2$	$1/2\rho_\infty V_\infty^3$
0.001	6.283×10^{1}	1.463×10^{4}	8.780×10^{7}
0.01	4.837×10^{0}	1.390×10^{3}	8.340×10^{6}
0.1	4.360×10^{-1}	1.449×10^{2}	8.695×10^{5}
1	4.506×10^{-2}	1.453×10^{1}	8.717×10^{4}
10	6.009×10^{-3}	1.378×10^{0}	8.269×10^{3}
100	1.109×10^{-3}	1.243×10^{-1}	7.456×10^{2}

Numerical Uncertainty

A major source of numerical uncertainty associated with applying both the DSMC and CFD techniques is the user defined grid; therefore, a brief discussion of this source of uncertainty specific to the present study is presented. As mentioned previously, the DAC DSMC requires a triangulated surface geometry description, which is placed in a Cartesian grid and the simulation is performed within the grid. One of the primary uncertainty sources is the grid in a high gradient region such as a shock wave or flow near the body. The DAC series reduces this uncertainty source by including a preprocessing code that produces an adapted Cartesian grid. Application of the regridding process is controlled by the user. For this study, multiple adaptations were performed to ensure that the grid in regions of large gradients and near the surface were dimensioned to less than the mean free path resolution. Sub-mean free path gridding is required to resolve completely the surface quantities with DSMC (For example, see Moss, et al.[7]).

For CFD, flow field convergence, which is a function of both the solution L_2 norm and the grid density, affects the solution uncertainty. The CFD solutions of the present study were advanced through a coarse, medium, and fine grid to accelerate convergence and allow a comparison of the solution at the various grid densities. After the solution was converged on the coarse grid, it was interpolated onto the finer grid and the solution converged again. The grid density change from the coarse to medium grid is accomplished by increasing the number of computational cells by a factor of 2 all directions; likewise, the change from a medium to fine grid is produced by increasing the number of cells by a factor of 2 in all computational directions. For the present CFD cases, when the L_2 norm decreased between 5 to 7 orders of magnitude and the L_2 norm, surface pressure, and heating became steady, the solution was assumed converged. In addition, when converged solutions on the medium grid, were compared with the fine grid solution, the stagnation pressure difference was less than about 2% and the stagnation heating less than about 5%.

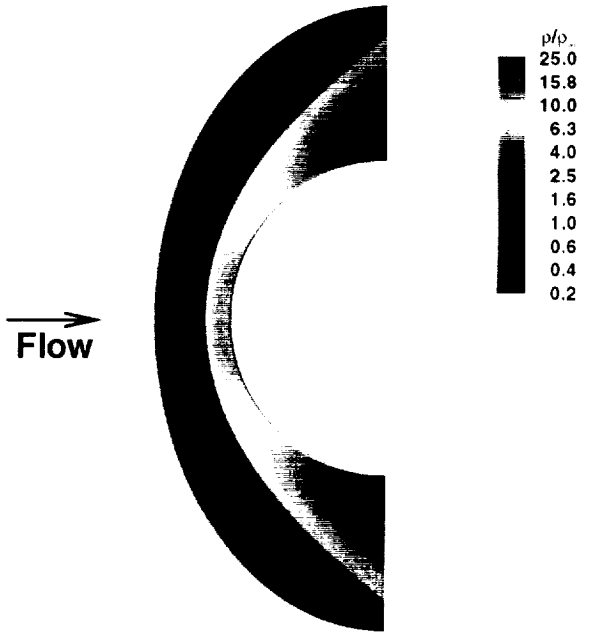

Fig. 3 Cylinder flow field density contours for $Kn_D = 0.001$ from CFD.

Density Contours

Density contours for the $Kn_D = 0.001$, 0.01, 10, and 100 cases are presented in this section for both the cylinder and sphere. These Knudsen number cases were chosen because they represent the end points of study ($Kn_D = 0.001$ and 100) and the cross over points where two techniques were applied ($Kn_D = 0.01$ and 10).

Cylinder

Shown as Figures 3, 4, 5, and 6 are the flow field contours for a cylinder at the $Kn_D = 0.001$, 0.01, 10, and 100, respectively, and the free stream conditions given in Table 1. For the continuum flow case (Figure 3), the CFD solution of the flow field shows a sharp bow

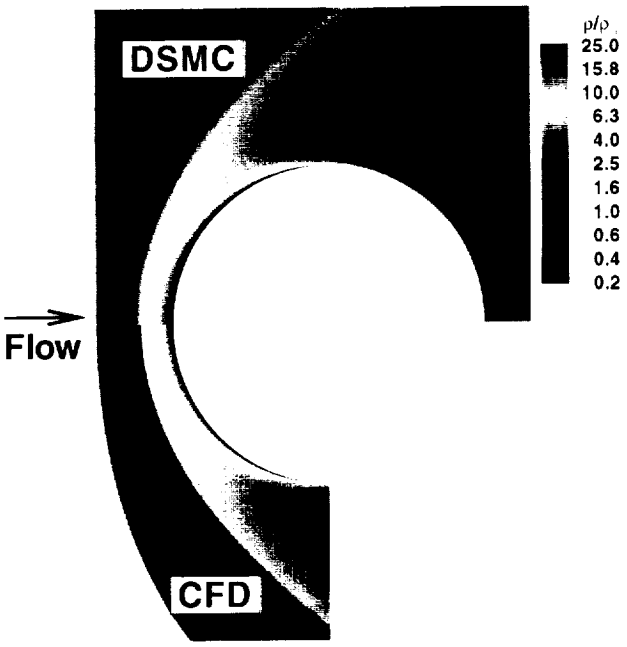

Fig. 4 Cylinder flow field density contours for $Kn_D = 0.01$ from DSMC and CFD.

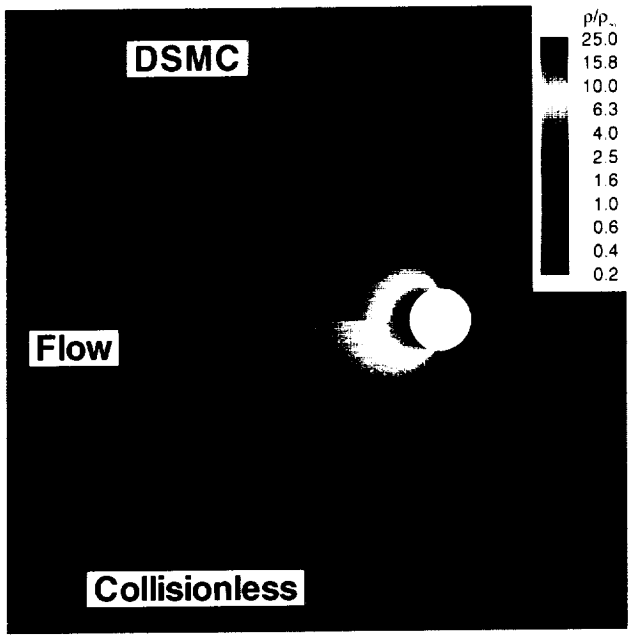

Fig. 5 Cylinder flow field density contours for $Kn_D = 10$ from DSMC and collisionless DSMC.

shock with a high density stagnation region. The contours also show that as the flow proceeds both above and below the cylinder, the density decreases because, away from the stagnation region, the flow is allowed to expand.

Shown as Figure 4 are the density contours for the $Kn_D = 0.01$ condition. At this Knudsen number, both DSMC and CFD solutions were obtained because the condition is near the transition from continuum to transitional flow. The flow field shown on the upper portion of the figure is taken from the DSMC solution and the one on the lower portion is taken from the CFD

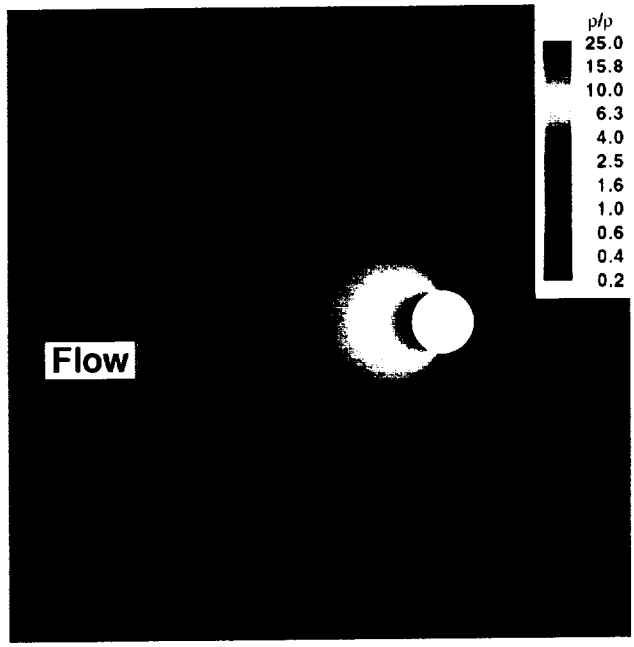

Fig. 6 Cylinder flow field density contours for $Kn_D = 100$ from collisionless DSMC.

solution. These density contours are very similar with the exception of the diffuse nature of the DSMC bow shock leading edge, which is most apparent where the two contours meet along the y/R = 0 line. Because the DSMC technique more closely simulates the probabilistic nature of the flow physics at this condition, the upper contour probably better describes the flow. Also, note that the DSMC solution models the flow about the cylinder including the wake region shadowed by the cylinder. A comparison of the DSMC and CFD flow field at the CFD outflow boundary (x/R = 0) shows little difference, which lends credence to not modeling the wake region with the CFD.

The next contours, shown in Figure 5, are at the $Kn_D = 10$ flow condition, which is near the transition between the transitional and free molecular flow regimes. The comparison shown on the figure is between a DSMC and collisionless DSMC solution. Because free molecular flow is collisionless, the DSMC code with the collision routine disabled properly represents a free molecular condition.

Figure 5 shows that for either case, no distinct bow shock is present, only a diffuse region with a gradual density increase as the flow approaches the cylinder. The collisionless DSMC solution for this Knudsen number has a higher density region further forward of the cylinder than the DSMC solution. The 2-D nature of the cylinder flow with no relief in the z-direction does not allow molecules to travel non-preferentially after a collision. Moreover, this effect shows that for the 2-D $Kn_D = 10$ flow condition, collisionless DSMC is not applicable to define this flow.

The final cylinder flow contour shown is Figure 6 for $Kn_D = 100$. This solution was produced using

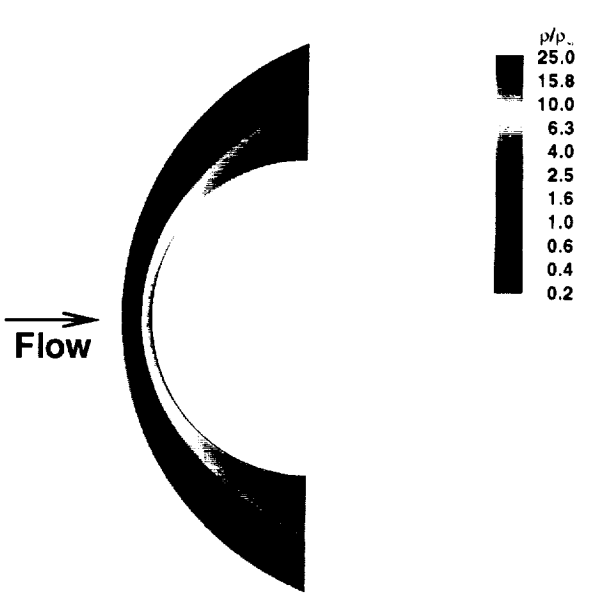

Fig. 7 Sphere flow field density contours for $Kn_D = 0.001$ from CFD.

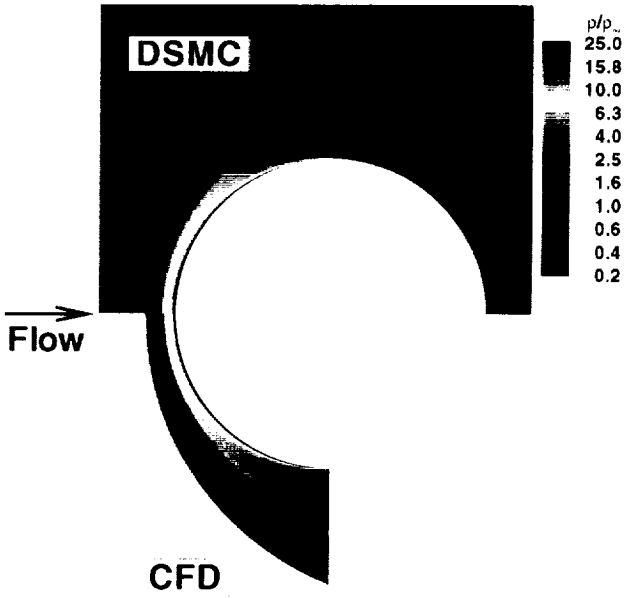

Fig. 8 Sphere flow field density contours for $Kn_D = 0.01$ from DSMC and CFD.

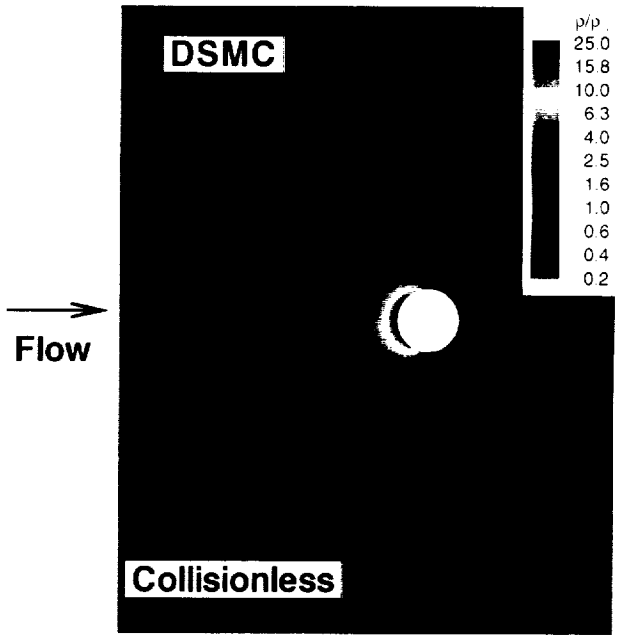

Fig. 9 Sphere flow field density contours for $Kn_D = 10$ from DSMC and collisionless DSMC.

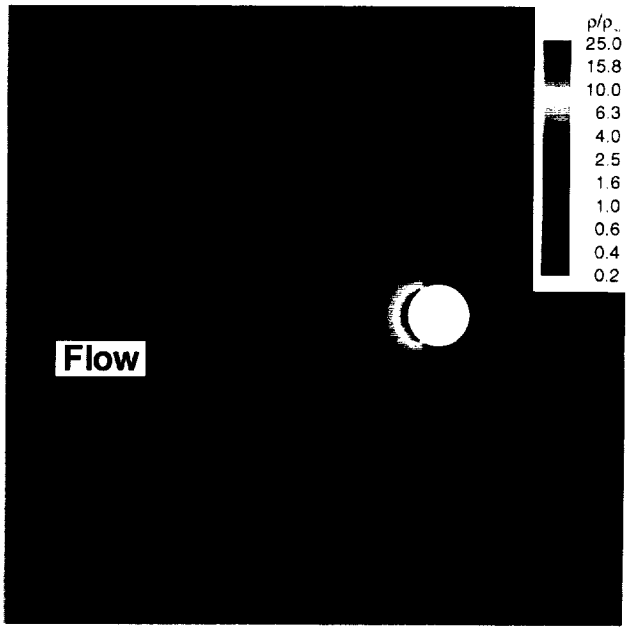

Fig. 10 Sphere flow field density contours for $Kn_D = 100$ from collisionless DSMC.

collisionless DSMC because the mean free path, λ, of the free stream is about 10 m, and a free molecular assumption for the 0.1 m diameter cylinder at this condition is appropriate. No prominent bow shock is shown in the figure, only a diffuse high density region extending forward of the cylinder.

Sphere

Similar to the cylinder contours, Figures 7, 8, 9, and 10 show density contours for the sphere at $Kn_D = 0.001$, 0.01, 10, and 100, respectively. The free stream conditions for these cases are taken from Table 1 and the flow field density shown in the figures is normalized by the free stream density given in the table.

Figure 7 shows the CFD flow field for the most continuum condition ($Kn_D = 0.001$). Note that a sharp bow shock is produced in front of the sphere as the flow encounters it. When compared with the cylinder flow field at the same Knudsen number (Figure 3), the sphere bow wave is closer to body because the spherical geometry provides a 3-D flow relief, thus allowing the closer bow shock.

For the $Kn_D = 0.01$ case, CFD and DSMC were

employed to produce the flow field solutions shown in Figure 8. The flow field at this free stream condition is near the transition between continuum and transitional flow. Note that a DAC DSMC axisymmetric solution was required for this case to provide the grid density needed to accurately describe the near wall flow gradients with sub mean free path resolution. As with the cylinder results, DSMC density contours are on the upper half of the figure and CFD contours are on the lower half. The DSMC bow shock is more diffuse at its leading edge than the CFD because, as discussed previously, the DSMC provides a better representation of this flow regime than the CFD. Again, the DSMC flow field includes the wake portion behind the sphere and, as was seen with the cylinder flow field, the CFD contours at the outflow boundary are similar to the DSMC contours at the some location.

The next density contours for the sphere are shown in Figure 9 for $Kn_D = 10$, which is near the Knudsen number between the transitional and free molecular flow regimes. Like the cylinder contours shown in Figure 5, the contours on the upper half of the figure are from the DSMC solution and the collisionless DSMC contours are on the lower half of the figure. The bow shock is not distinguished with a sharp gradient associated with continuum flow, and the density contours in front of the sphere gradually rise as the flow moves closer to the sphere. Unlike the cylinder results where the flow field is disturbed further upstream, a comparison of the two sphere density contours on Figure 9 shows similarity. The 3-D flow relief of the sphere simulation allows the collisionless technique to better model this condition than the 2-D collisionless simulation used for the cylinder. Therefore, the use of a collisionless simulation at this Knudsen number is better justified for a 3-D simulation.

The $Kn_D = 100$ density contour figure for the sphere (Figure 10) is the final one presented in this section. Collisionless DSMC is employed to produce a solution for this free molecular flow field. Compared to the 2-D cylinder density contours (See Figure 6.), the sphere contours do not extend as far forward as with the cylinder. As discussed previously, the nature of the sphere simulation allows the molecules, which encounter the sphere, to reflect into a 3-D space, thus lessing the forward reflected molecules and better modeling the flow.

Stagnation Streamline Results

The variation of normalized temperature and density along the stagnation streamline in the flow direction for each of the GASP CFD, DAC DSMC, and collisionless DAC DSMC cases, given in Table 2, is presented in this section. The cylinder and sphere results are grouped from the continuum to the most rarefied condition in the following order: first, temperature and density for the CFD cases ($Kn_D = 0.001$ and 0.01); second, temperature and density for the CFD and DSMC cases near the transition between the continuum and transitional regimes ($Kn_D = 0.01$); third, temperature and density for the DSMC cases ($Kn_D = 0.01$, 0.1, 1, and 10); next, temperature and density for DSMC and collisionless DSMC near the transition between transitional and free molecular flow ($Kn_D = 10$); then, temperature and density for collisionless DSMC ($Kn_D = 10$ and 100); the maximum atomic oxygen and nitrogen; and finally, overall, translational, rotational, and vibrational temperature distributions for $Kn_D = 0.1$.

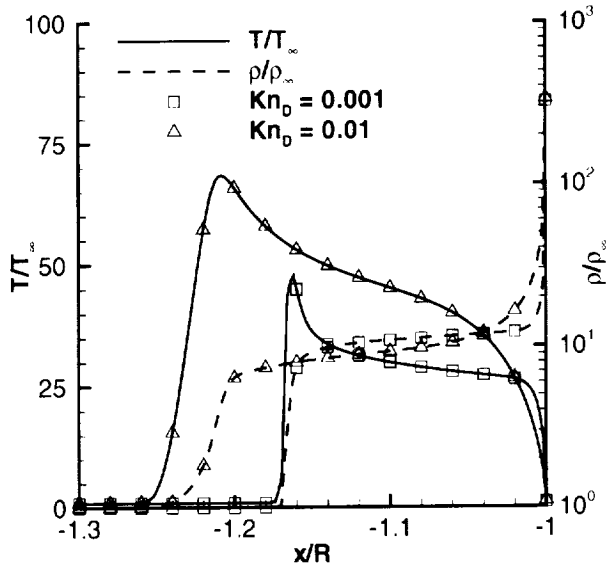

Fig. 11 Cylinder stagnation streamline flow field properties for $Kn_D = 0.001$ and $Kn_D = 0.01$ from CFD.

For the cylinder CFD cases, Figure 11 shows, for increasing Knudsen number, or decreasing free stream density, shock standoff distance increases and the temperature and density gradient at the leading edge of the bow shock decreases. Also, for the $Kn_D = 0.01$ case, the initial temperature rise before encountering the bow shock occurs earlier, or further from the body, than for the $Kn_D = 0.001$ case showing the effect of a less continuum like flow. In addition, the maximum normalized temperature for $Kn_D = 0.01$ case is larger than for $Kn_D = 0.001$.

The sphere CFD results at the same conditions are given as Figure 12. Although the sphere flow field properties show the same trends as those of the cylinder, they occur much closer to the surface because the 3-D relief of the flow about the sphere. Also, note that for both the cylinder and sphere cases, a sharp gradient in both temperature and density occurs near the wall because of the imposed 300 K wall temperature.

Next, at $Kn_D = 0.01$, a comparison between the CFD and DSMC stagnation streamline temperature

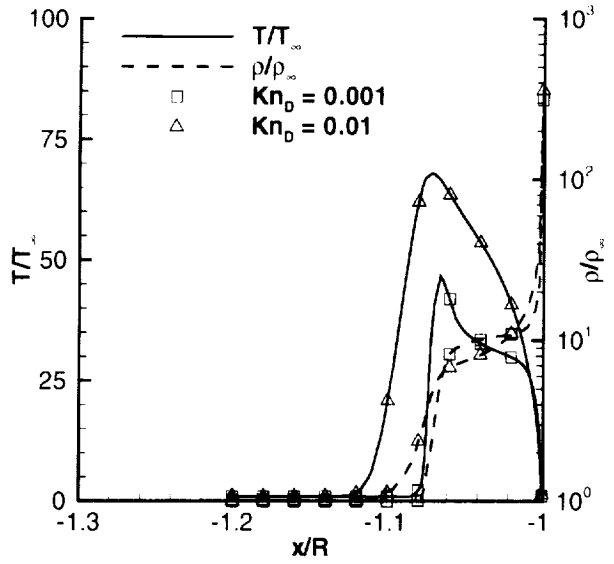

Fig. 12 Sphere stagnation streamline flow field properties for $Kn_D = 0.001$ and $Kn_D = 0.01$ from CFD.

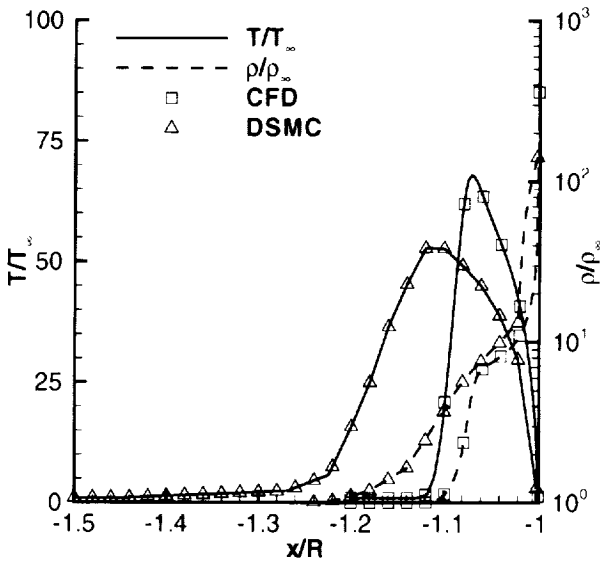

Fig. 14 Sphere stagnation streamline flow field properties for $Kn_D = 0.01$ from CFD and DSMC.

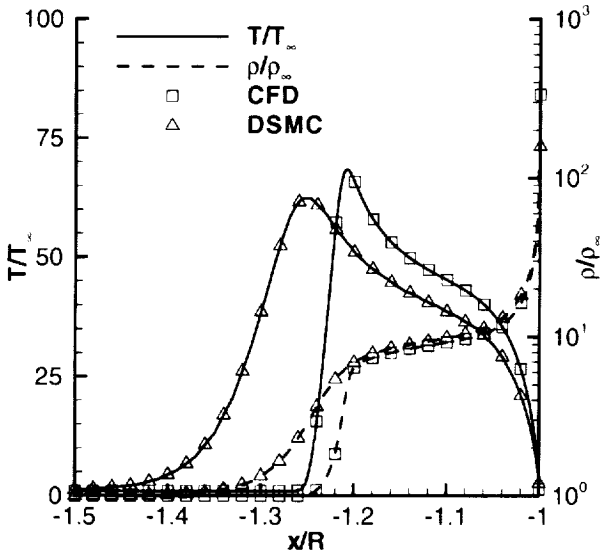

Fig. 13 Cylinder stagnation streamline flow field properties for $Kn_D = 0.01$ from CFD and DSMC.

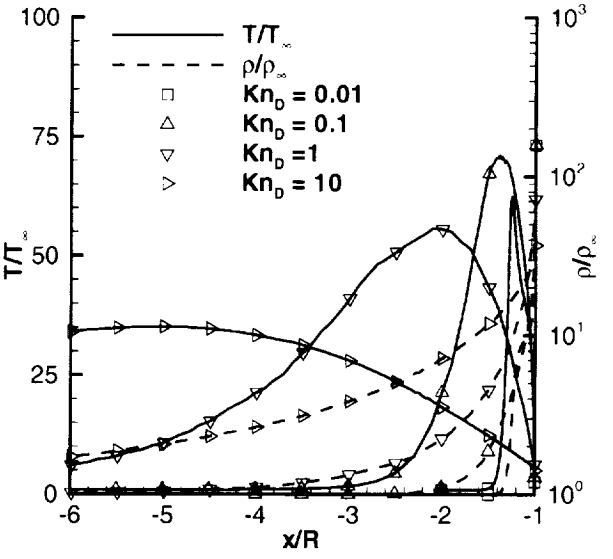

Fig. 15 Cylinder stagnation streamline flow field properties for $Kn_D = 0.01$ to $Kn_D = 10$ from DSMC.

and density for the cylinder, shown in Figure 13, and for the sphere, shown in Figure 14, is presented. The figures show that temperature and density gradients for DSMC are less than those for CFD, which was also shown in the density contour comparisons at the same Knudsen number (See, for example, Figures 4 and 8 for the cylinder and sphere, respectively.). Note, however, that the comparison for the cylinder is better than that for the sphere – the maximum temperature rise and the temperature and density wall gradient are closer. Even though the CFD and DSMC cylinder results are in better agreement than those for the sphere, in general, the proper treatment of the solution at this condition is by performing DSMC, which allows for a more realistic shock wave structure to evolve as compared to the CFD calculation.

Figures 15 and 16 show the normalized temperature and density along the stagnation streamline for the cylinder and sphere, respectively, over the Knudsen number range $0.01 \leq Kn_D \leq 10$ as predicted by the DSMC technique. For both geometries, as the flow is initially affected by the body, the tempera-

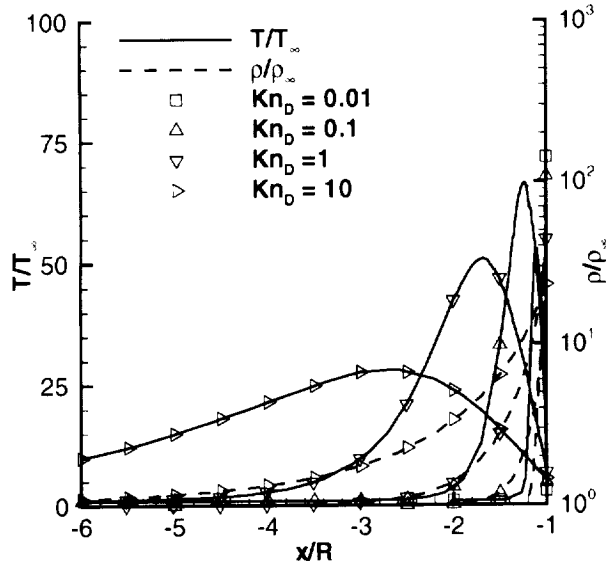

Fig. 16 Sphere stagnation streamline flow field properties for $Kn_D = 0.01$ to $Kn_D = 10$ from DSMC.

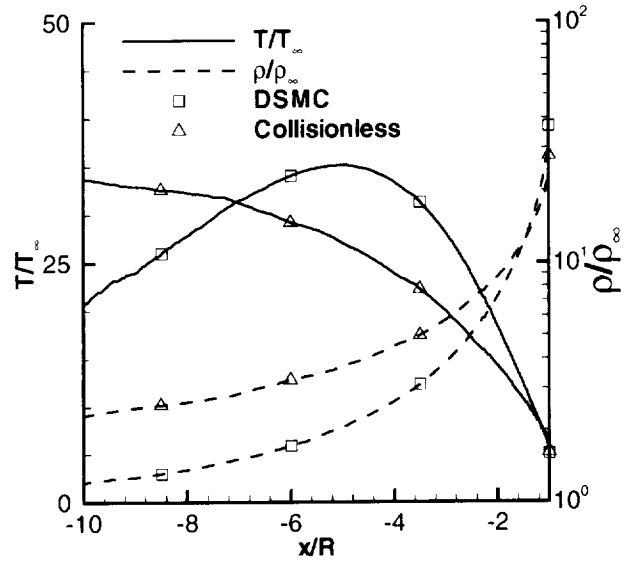

Fig. 17 Cylinder stagnation streamline flow field properties for $Kn_D = 10$ from DSMC and collisionless DSMC.

ture and density increase, but the gradient decreases as the Knudsen number increases. Also, the maximum overall temperature for $Kn_D = 0.1$, shown in both figures, is greater than for the other Knudsen numbers. Therefore, the thermal nonequilibrium aspects of the $Kn_D = 0.1$ case will be examined in greater detail subsequently.

A comparison between DSMC and collisionless DSMC for a cylinder at $Kn_D = 10$ is shown next as Figure 17. As discussed previously with the comparison of Figure 5, the collisionless DSMC allows reflected molecules to return upstream without colliding with downstream moving molecules, which causes higher upstream density contours than the DSMC case. A comparison of the temperature distributions shows the collisionless DSMC temperature is much greater than that of the DSMC (See Figure 17.). This is because the collisionless overall temperature shown on the figure is only composed of the translational component, a gross measure of the average molecular speed, which for this case, has contributions from molecules streaming in both directions; therefore, showing the collisionless assumption for the cylinder at this condition is not appropriate.

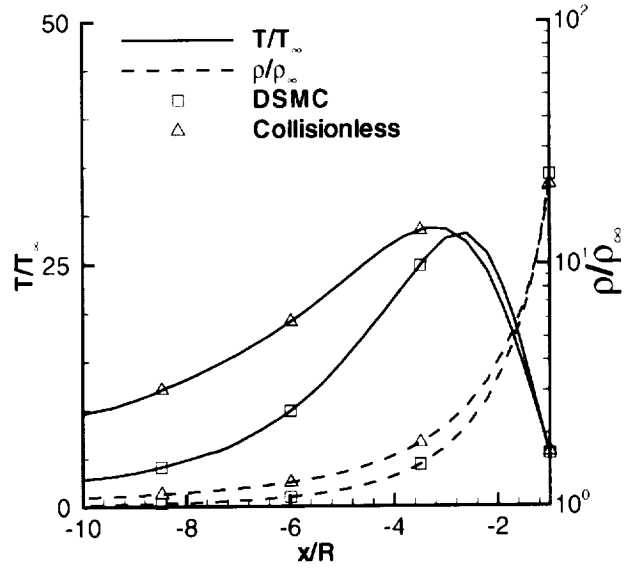

Fig. 18 Sphere stagnation streamline flow field properties for $Kn_D = 10$ from DSMC and collisionless DSMC.

The comparison for the sphere at the same conditions is shown as Figure 18. Unlike the cylinder, the sphere streamline temperature results for the two techniques are in much better agreement. In addition, the sphere density distributions are in good agreement, whereas, the cylinder density distributions shown in Figure 17 are not similar. Overall, the cylinder and sphere results show the difference between imposing a 2-D collisionless DSMC flow assumption, which is very restrictive, and 3-D collisionless DSMC at this Knudsen number.

The final comparison along the stagnation line is between the collisionless DSMC results at $Kn_D = 10$ and 100, which are shown on Figures 19 and 20, respectively, for the cylinder and sphere. Although, for the cylindrical flow field, the $Kn_D = 10$ collisionless DSMC has been shown not to be appropriate, it is included as a reference to compare with the $Kn_D = 100$ case. The cylinder temperature and density distri-

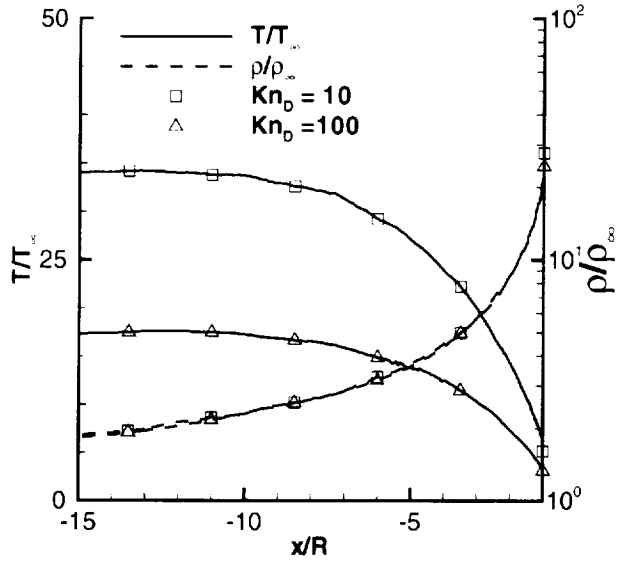

Fig. 19 Cylinder stagnation streamline flow field properties for $Kn_D = 10$ and $Kn_D = 100$ from collisionless DSMC.

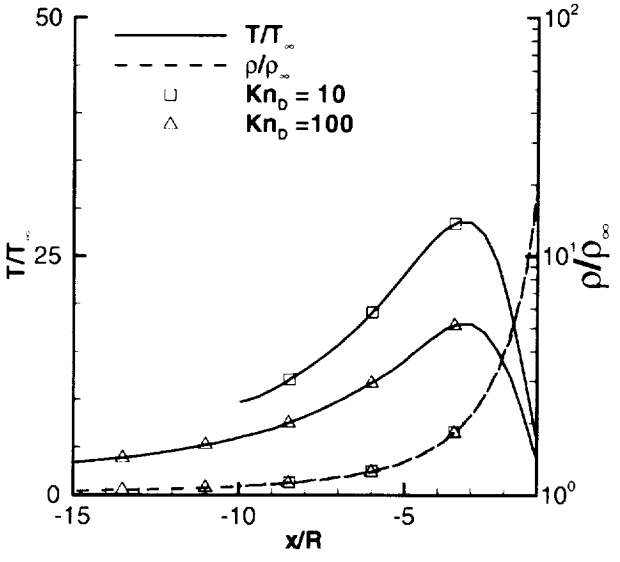

Fig. 20 Sphere stagnation streamline flow field properties for $Kn_D = 10$ and $Kn_D = 100$ from collisionless DSMC.

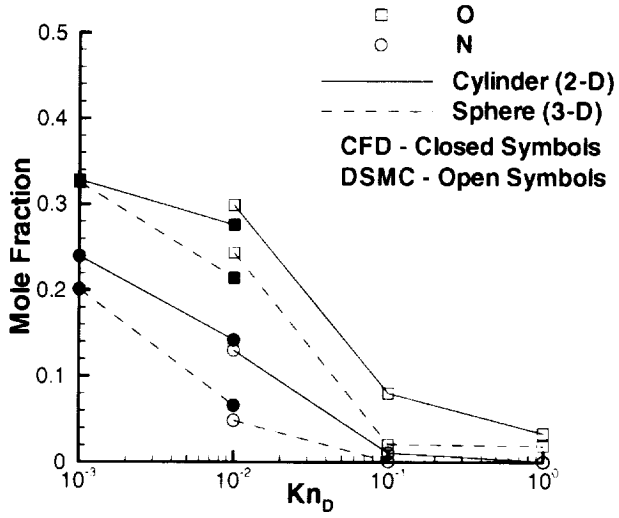

Fig. 21 Maximum atomic oxygen and nitrogen mole fraction along stagnation streamline.

bution comparison shows that both Knudsen number cases exhibit the same behavior over the x/R range shown; that is, the overall temperature drops as the flow encounters the cold wall. Also, the density distributions are nearly the same.

The sphere results, shown in Figure 20, however, have a different temperature distribution, which rises to a maximum value close to the sphere, then drops as the flow encounters the cold wall. This rise and fall is characteristic of three dimensional scattering of the molecules from the sphere surface.

The maximum mole fraction of atomic oxygen and nitrogen along the stagnation streamline is presented next as Figure 21. This figure is included to show the degree of chemical nonequilibrium along the stagnation streamline for Knudsen numbers over the range $0.001 \leq Kn_D \leq 1$. The figure includes both the CFD and DSMC results for the cylinder and sphere. Line segments are also included between the calculated points in the figure only to distinguish the cylinder from the sphere results, not to provide an interpolation between the data points. The trend shown in the figure is that a maximum O and N in the shock layer occurs for $Kn_D = 0.001$, with a significant O mole fraction concentration (greater than 30%). Note that the O mole fraction is greater than the N because O_2 dissociates at a lower energy level than N_2. Also, the cylinder flow field shows a greater degree of dissociation than the sphere because the cylinder shock layer is thicker, which provides a greater residence time for the flow dissociation to proceed. In addition, the figure shows that for $Kn_D \geq 0.1$, chemical dissociation becomes less significant in the flow calculation. Therefore, it is essential to include a chemistry model in a flight environment stagnation flow calculation for the more continuum-like portion of the transitional regime, that

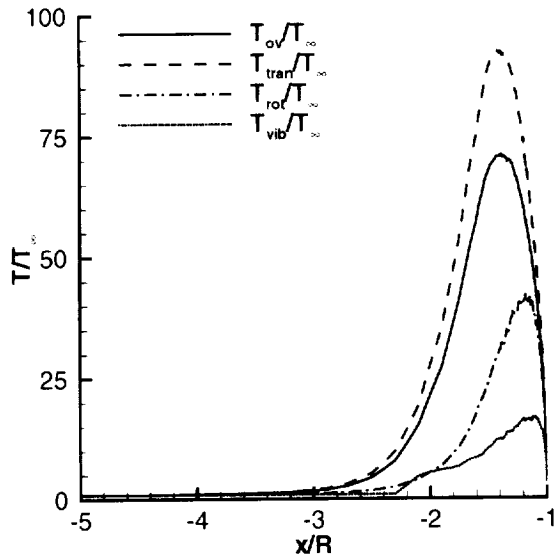

Fig. 22 Cylinder stagnation streamline flow field temperature for $Kn_D = 0.1$ from DSMC.

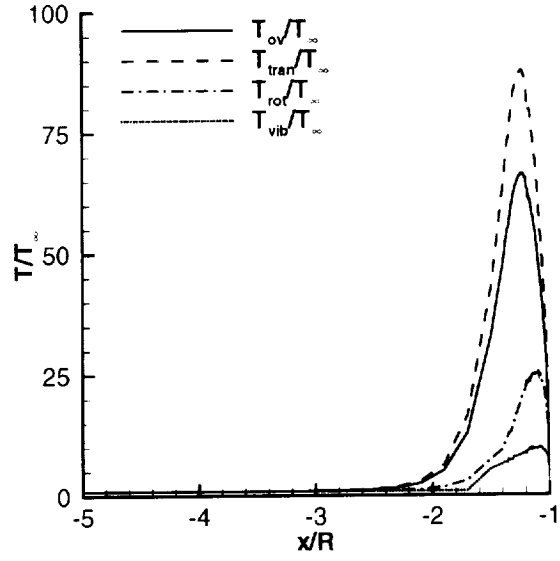

Fig. 23 Sphere stagnation streamline flow field temperature for $Kn_D = 0.1$ from DSMC.

is, for the range $Kn_D < 1$.

As previously indicated, the maximum temperature along the stagnation streamline for the $Kn_D = 0.1$ case, shown for the cylinder and sphere in Figures 15 and 16, respectively, was greater than for the other Knudsen number cases and may show the effects of thermal nonequilibrium; therefore, the overall, translational, rotational, and vibrational temperature components for these two cases are presented and discussed. Also note, as shown in Figure 21 and discussed previously, chemical nonequilibrium effects are present, but not significant for this case.

Results for the cylinder are shown in Figure 22, and for the sphere, in Figure 23. The extent of thermal nonequilibrium is indicated by the temperature profiles for each energy mode. Note that for this case, as shown in the figures, all three energy modes are activated inside the shock layer as the flow approaches the body. The energy distribution of the flow is related to the translational and internal (rotational and vibrational) temperatures. The cylinder flow has a greater rotational and vibrational temperature than the sphere flow (Compare Figures 22 and 23.), perhaps because the thicker cylinder shock layer allows a greater degree of equilibration than the sphere shock layer, which may, in part, be chemically frozen and have a higher degree of thermal nonequilibrium because of the thinner sphere shock layer. In any event, to accurately predict this flow field, a technique, which accounts for local thermal nonequilibrium effects of the flow, is needed. In addition, Cuda and Moss[8] and Moss, et al.[9] found significant thermal nonequilibrium effects from bodies at flight conditions near the same altitude as for the present $Kn_D = 0.1$ case.

Although not presented graphically, an examination of the various temperature modes for the cylinder and sphere at the $Kn_D = 0.01$, 1, and 10 conditions was performed. At $Kn_D = 0.01$, the flow in the shock layer was nearly in thermal equilibrium, and at the higher altitudes (Kn_D = 1 and 10), the internal energy modes were essentially frozen at the free stream condition and were not in thermal equilibrium.

Stagnation Point Results

Presented are the stagnation point values from the 22 cases that are shown on Table 2. These single point values of pressure and heating are given in coefficient form as C_p and C_H with the normalization constants taken from Table 3. The Knudsen number range of the data is $0.001 \leq Kn_D \leq 100$, which spans from the continuum to the free molecular regime for the cylinder and sphere conditions, and defines the C_p and C_H bridging relations for the two geometries over the Knudsen number range. Figure 24 shows the cylinder results, and Figure 25 shows the sphere results.

Some of the results from the 3-D DSMC DAC code of LeBeau[3] that are presented in these figures are anchored by results from the 2-D/axisymmetric G2 code of Bird.[2] A comparison of pressure and heat transfer coefficient is provided at $Kn_D = 0.01$, 1, and 10 for the cylinder and sphere, respectively, in Figures 24 and 25. The pressure coefficient comparisons at $Kn_D = 0.01$ are in excellent agreement and at the other two Knudsen numbers are in good agreement for both the cylinder and sphere. The heat transfer coefficient, however, is in excellent agreement for all of the cases. Based on this, the 3-D DAC DSMC is shown to provide comparable stagnation pressure and heating results as the 2-D/axisymmetric G2 code.

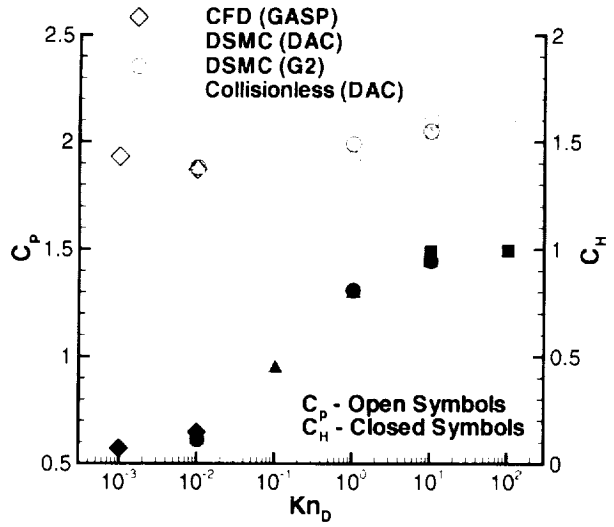

Fig. 24 Comparison of maximum cylinder C_p and C_H at various Kn_D from different techniques.

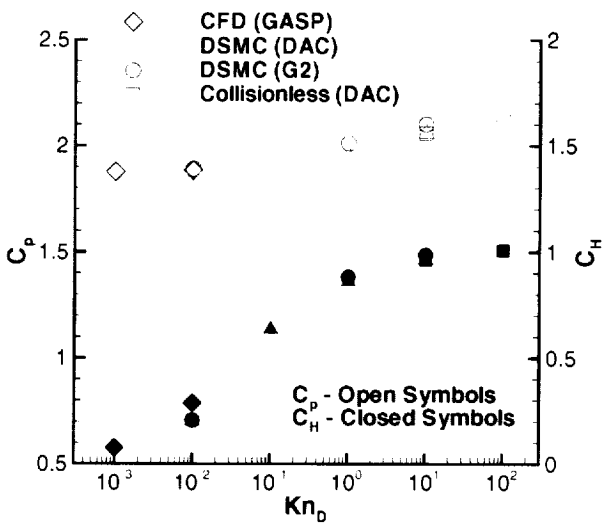

Fig. 25 Comparison of maximum sphere C_p and C_H at various Kn_D from different techniques.

The pressure coefficient for both the cylinder and sphere, shown in Figures 24 and 25, respectively, starts at a continuum value of about $C_p = 1.9$ at $Kn_D = 0.001$ and increases to a value of about 2.1 at the free molecular condition ($Kn_D = 100$). There is a noticeable difference between the cylinder and sphere C_p at the end points of the data where the cylinder results are closer to $C_p = 2$ than the sphere results. Also, there is a dip in the cylinder C_p value at $Kn_D = 0.01$. Moss, et al[10] show a dip in drag coefficient at about the same Knudsen number for the Pathfinder aeroshell shape. In addition, the collisionless DSMC cylinder result at $Kn_D = 10$ is higher than the DSMC result, but for the sphere, they are nearly the same. As discussed above and shown by comparisons in Figures 17 and 18, the reason the sphere DSMC and collisionless DSMC results more closely match is that the 3-D flow field of the sphere is better modeled than that of the cylinder.

Heat transfer coefficient for the cylinder and sphere is now discussed. For both geometries, the range of heat transfer coefficient is $0.1 \leq C_H \leq 1$ from the continuum ($Kn_D = 0.001$) to the free molecular ($Kn_D = 100$) regime, respectively. In addition, the cylinder C_H rise lags the sphere C_H rise with increasing Kn_D by about 1/2 an order of magnitude. This may be because the sphere shock layer is thinner and closer to the body with attendant higher gradients. These higher gradients in flow properties promote rarefaction effects more quickly than with the thicker cylinder shock layer with longer flow resident time scale for energy relaxation. At $Kn_D = 0.01$, the point where both CFD to DSMC solutions were obtained, the CFD C_H is larger for both the sphere and cylinder; however, the sphere CFD result is greater than the cylinder result, which is close to the DSMC result. This may show that CFD can provide an adequate cylinder stagnation heating estimate at $Kn_D = 0.01$, but cannot for the sphere. In addition, previous studies that provide CFD and DSMC solutions as a function of Knudsen number show that the CFD predictions are greater than DSMC predictions at the continuum transition (For example, see Cuda and Moss[8] and Gupta.[11]). Based on the results at $Kn_D = 0.01$ where both CFD to DSMC techniques were implemented, CFD may be used to obtain stagnation values for the cylinder, but, for the sphere, DSMC is needed.

At $Kn_D = 10$, which is the condition that both the DSMC and collisionless DSMC solutions were obtained, the collisionless DSMC cylinder and sphere results are greater than the DSMC with the difference between the cylinder results greater than with sphere results, which have little difference. Because both sphere stagnation heating results are close at the $Kn_D = 10$ condition and the cylinder results are not, a change in solution methods from DSMC to collisionless DSMC is better justified at this condition for the sphere than for the cylinder. Also, for a 3-D blunt configuration, Moss, et al.[10] show that free molecular flow begins at a Knudsen number of order 10.

Concluding Remarks

CFD, DSMC, and collisionless DSMC were utilized to provide solutions for a cylindrical and spherical geometry at reentry flight conditions, which span the Knudsen number range $0.001 < Kn_D < 100$. In particular, state-of-the-art computer programs are exercised for this problem to assess the applicability. Density contour comparisons, stagnation point streamline temperature and density distributions, and stagnation point values are shown for most of the cases. In addition, a comparison between 2-D/axisymmetric G2 results and 3-D DAC results is provided to anchor the 3-D DAC results; The results at the stagnation point

compare well and show the 3-D DAC DSMC is equivalent to the G2 DSMC.

At $Kn_D = 0.01$, near the continuum change to the transitional regime, CFD and DSMC solutions were obtained. For both the cylinder and sphere flow, CFD and DSMC flow fields differ, with the DSMC shock layer extending further from the surface. However, unlike the sphere results, the CFD and DSMC cylinder stagnation point values are nearly the same. Similarly, at $Kn_D = 10$, the DSMC and collisionless DSMC are compared near the change from the transitional to the free molecular regimes. Neither the flow field nor the surface quantities for the cylinder compare well between the DSMC and collisionless DSMC. However, the spherical flow results, which properly simulate the 3-D nature of the $Kn_D = 10$ condition, match more closely.

Chemical and thermal nonequilibrium effects were identified by examining the atomic oxygen and nitrogen concentration and the translational, rotational, and vibrational temperature components along the stagnation streamline for various cases. For the flight condition in the transitional regime, chemical nonequilibrium effects are significant at $Kn_D = 0.001$ and should be included for calculations where $Kn_D < 1$. Thermal nonequilibrium was also shown to be important, especially for $Kn_D \geq 0.1$.

In addition, the bridging of the cylindrical and spherical stagnation point pressure and heating over the $0.001 \leq Kn_D \leq 100$ is presented. For the conditions of the study, pressure coefficient varies little from a value of $C_p = 2$; however, heat transfer coefficient varies from about 0.1 at the continuum limit to 1 at the free molecular limit.

Acknowledgments

The authors acknowledge the help from and useful discussions with Mr. Gerald LeBeau of NASA Johnson Space Center about the DAC code. Dr. Ramadas Prabhu of Lockheed Martin Engineering & Services Corporation assisted in generating some of the surface triangulation using the GridTool and FELISA programs. Also, Dr. Reece Neel of AeroSoft Corporation provided a 3-D sphere grid, which was modified for the present study, and made useful suggestions about running GASP with finite rate chemistry. Lastly, Mr. Steven Alter of NASA Langley Research Center was helpful in applying his VGM program to provide high quality CFD grids.

References

[1]Anderson, D. A., Tannehill, J. C., and Pletcher, R. H., *Computational Fluid Mechanics and Heat Transfer*, Hemisphere Publishing Corporation, New York, 1984.

[2]Bird, G. A., *Molecular Gas Dynamics and the Direct Simulation of Gas Flows*, Clarendon Press, Oxford, 1994.

[3]LeBeau, G. J., "A Parallel Implementation of the Direct Simulation Monte Carlo Method," *Computer Methods in Applied Mechanics and Engineering, Parallel Computational Methods for Flow Simulation and Modeling*, Vol. 174, 1999, pp. 319–337.

[4]Bird, G. A., *DSMC Computation of Two-Dimensional or Axially-Symmetric (G2) or Three-Dimensional with Axially-Symmetric Grid (A3) Rarefied Flows, The G2/A3 Program System Users Manual, Version 1.8*, G.A.B. Consulting Pty Ltd, Killara, Australia, March 1992.

[5]AeroSoft, *GASP Version 3, The General Aerodynamic Simulation Program, Computational Flow Analysis Software for the Scientist and Engineer, User's Manual*, AeroSoft, Inc., May 1996.

[6]COESA, *U. S. Standard Atmosphere, 1976*, NOAA, NASA, USAF, Washington, D.C., October 1976.

[7]Moss, J. N., Rault, D. F. G., and Price, J. M., *AIAA Progress in Astronautics and Aeronautics, Rarefied Gas Dynamics: Space Science and Engineering*, Vol. 160, chap. Direct Monte Carlo Simulations of Hypersonic Viscous Interactions Including Separations, AIAA, 1993, pp. 209–220.

[8]Cuda Jr., V. and Moss, J. N., "Direct Simulation of Hypersonic Flows Over Blunt Slender Bodies," *Journal of Thermophysics and Heat Transfer*, Vol. 1, No. 2, April 1986, pp. 97–104.

[9]Moss, J. N., Cuda Jr., V., and Simmonds, A. L., "Nonequilibrium Effects for Hpersonic Transitional Flows," AIAA Paper 87-0404, January 1987.

[10]Moss, J. N., Blanchard, R. D., G., W. R., and Braun, R. D., "Mars Pathfinder Rarefied Aerodynamics: Computations and Measurements," *Journal of Spacecraft and Rockets*, Vol. 36, No. 3, May–June 1999, pp. 330–339.

[11]Gupta, R. N. and Simmonds, A. L., "Hypersonic Low-Density Solutions of the Navier-Stokes Equations with Chemical Nonequilibrium and Multicomponent Surface Slip," AIAA Paper 86-1349, June 1986, AIAA/ASME 4th Joint Thermophysics and Heat Transfer Conference.